some regions but not as well in others.

A map of the difference $\Delta\Sigma_{\text{eff}}$ between this linear relation and the calculated Σ_{eff} points (Fig. 3) reflects the implied abundance of neutron absorbers other than Fe and Ti (Fig. 4). The highest values are found over the rim of the Imbrium basin, including the Apennine mountains in the east up through the Alps, across to the Jura mountains in the west, down through the Aristarchus plateau and through the Fra Mauro formation to the south. LP gamma-ray spectrometer maps show that these regions also have high Th and K concentrations (*13*). This similarity implies that the absorbing species are affiliated with the incompatible elements found in KREEP; the correlation coefficient between the gamma-ray spectrometer Th data (*13*) and $\Delta\Sigma_{\text{eff}}$ is 0.93. The values of $\Delta\Sigma_{\text{eff}}$ are consistent with the range (10×10^{-4} to 42×10^{-4} cm^2/g) of Gd and Sm contributions listed in Table 1. The K in KREEP plays only a very minor role in Σ_{eff} (Table 1). Therefore, we conclude that $\Delta\Sigma_{\text{eff}}$ reflects primarily the concentration of Gd and Sm and, thus, is a tracer for KREEP.

The estimated thermal neutron macroscopic absorption coefficient that would be expected on the basis of concentrations of Fe and Ti derived from CSR data, coupled with an estimate of Ca concentrations, is in reasonable agreement with the LP neutron spectrometer results. Discrepancies arise in regions that have significant levels of KREEP, where Gd and Sm are major thermal neutron absorbers. Thus, the CSR method appears to be a reliable technique for obtaining FeO and TiO$_2$ abundances moonwide. The inferred KREEP-rich regions form a ring around the Imbrium impact site and are directly related to either excavation of this lower crustal chemistry or to volcanism that extruded KREEP-rich lava on the surface. On the other hand, the much larger, deeper South Pole–Aitken impact basin shows little KREEP enhancement (*14*). This result appears to confirm the uniqueness of the Imbrium lower crustal chemistry and suggests that the moon may have considerable regional compositional heterogeneity at depth.

References and Notes

1. P. G. Lucey, G. J. Taylor, E. Malaret, *Science* **268**, 1150 (1995).
2. P. G. Lucey, D. T. Blewett, J. R. Johnson, G. J. Taylor, B. R. Hawke, *Lunar Planet Sci.* **XXVII**, 781 (1996).
3. D. T. Blewett, P. G. Lucey, B. R. Hawke, B. L. Jolliff, *J. Geophys. Res.* **102**, 16319 (1997).
4. P. G. Lucey, D. T. Blewett, B. R. Hawke, *ibid.* **103**, 3679 (1998).
5. P. E. Clark and A. Basu, *Proc. Lunar Planet. Sci. Conf.* **29**, 1501 (1998). Olivine is the likeliest mineral to be underrepresented in the results from analysis of spectral data.
6. W. C. Feldman *et al.*, *Science*, **281** 1496 (1998).
7. W. C. Feldman *et al.*, *ibid.*, p. 1489 (1998).
8. D. M. Drake, W. C. Feldman, B. M. Jakosky, *J. Geophys. Res.* **93**, 6353 (1988).
9. R. C. Reedy *et al.*, *Meteorit. Planet. Sci.* **33** (suppl.), A127 (1998).
10. L. A. Haskin and P. H. Warren, in *Lunar Sourcebook*, G. H. Heiken, D. T. Vaniman, B. M. French, Eds. (Cambridge Univ. Press, New York, 1991), pp. 367–474, figure 8.3. The inverse correlation between FeO and CaO is principally due to variations in the abundance of anorthite, a Ca-rich and Fe-poor plagioclase. At higher FeO contents where the correlation flattens, the rocks are typically mare basalts, which contain less anorthite but more calcic pyroxenes.
11. R. Lingenfelter, E. H. Canfield, V. E. Hampel, *Earth Planet. Sci. Lett.* **16**, 355 (1972).
12. W. C. Feldman, R. C. Reedy, D. S. McKay, *Geophys. Res. Lett.* **18**, 2157 (1991).
13. D. J. Lawrence *et al.*, *Science* **281**, 1484 (1998).
14. *Note added in proof*: The fast neutron data suggest that the CSR FeO abundances in South Pole–Aitken basin may be overestimated. If so, then it is likely that Gd and Sm abundances are higher there than we have estimated, and the basin is richer in incompatible elements than we have suggested.
15. This research was partially supported by NASA through a subcontract from Lockheed-Martin Corporation. We thank R. Reedy and D. Vaniman for discussions, P. Spudis and another referee for helpful and thorough reviews, and D. Thomsen for maps of lunar surface features. This work was performed under the auspices of the U.S. Department of Energy.

13 July 1998; accepted 7 August 1998

Fluxes of Fast and Epithermal Neutrons from Lunar Prospector: Evidence for Water Ice at the Lunar Poles

W. C. Feldman,* S. Maurice, A. B. Binder, B. L. Barraclough, R. C. Elphic, D. J. Lawrence

Maps of epithermal- and fast-neutron fluxes measured by Lunar Prospector were used to search for deposits enriched in hydrogen at both lunar poles. Depressions in epithermal fluxes were observed close to permanently shaded areas at both poles. The peak depression at the North Pole is 4.6 percent below the average epithermal flux intensity at lower latitudes, and that at the South Pole is 3.0 percent below the low-latitude average. No measurable depression in fast neutrons is seen at either pole. These data are consistent with deposits of hydrogen in the form of water ice that are covered by as much as 40 centimeters of desiccated regolith within permanently shaded craters near both poles.

The moon is depleted in all volatile elements compared with Earth (*1*). However, water was brought to the moon by comets and asteroids and was formed by the reduction of FeO in lunar materials by solar wind hydrogen, and some juvenile water may have been released from the lunar interior over billions of years (*2*, *3*). Studies of the transport of such water over the lunar surface after its release indicate that 20 to 50% should be retained as frozen water ice within permanently shaded craters near both poles (*2*–*6*). However, losses due to meteoritic bombardment (*3*) and erosion due to particle sputtering (*7*), or photodissociation by interstellar hydrogen Lyman-α (*8*), may exceed the accretion rate preventing the development and retention of permanent ice deposits at the poles.

The interpretation of anomalously large intensities of same-sense polarized radar echoes that are localized to permanently shaded craters near the poles of Mercury (*9*–*11*) as caused by deposits of nearly pure water ice suggests that similar deposits should also exist on the moon. Although a report of a possible detection of water ice on the moon with Clementine data (*12*) supports this suggestion, it is not universally accepted (*13*, *14*). We address the question of lunar water ice using epithermal- and fast-neutron data measured using the Lunar Prospector (LP) neutron spectrometer (NS).

Expected signature of H. A unique identification of chemical species enriched in hydrogen and a characterization of their spatial distribution are possible through measurement of neutron flux spectra (*15*, *16*). The magnitude of this effect at 100-km altitude is illustrated with simulated neutron flux spectra (Fig. 1). The different curves give neutron lethargy, $L(E)$, as a function of energy, E, for ferroan-anorthosite (FAN, a major type of soil or regolith in the lunar highlands) containing various admixtures of H$_2$O (*17*). There are three general energy ranges that

---

W. C. Feldman, B. L. Barraclough, R. C. Elphic, D. J. Lawrence, Los Alamos National Laboratory, MS D-466, Los Alamos, NM 87545, USA. S. Maurice, Observatoire Midi-Pyrenees, 14 avenue Edouard Belin, 31400 Toulouse, France. A. B. Binder, Lunar Research Institute, 1180 Sunrise Drive, Gilroy, CA 95020, USA.

*To whom correspondence should be addressed. E-mail: wfeldman@lanl.gov

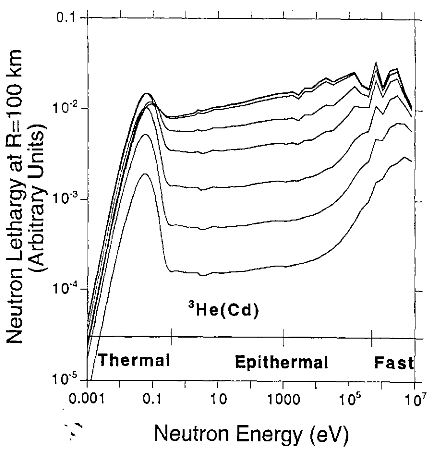

Fig. 1. Simulated neutron lethargy-energy spectra for a FAN regolith containing various weight percent admixtures of H_2O (*w*). These spectra were generated with the ONEDANT part of the DANTSYS code system (*27*) as discussed in (*16*). From top to bottom, the spectra correspond to mass fractions of H_2O (*w*) of 0, 0.01, 0.1, 1, 3, 10, 30, and 100%, respectively. *R*, altitude of spacecraft.

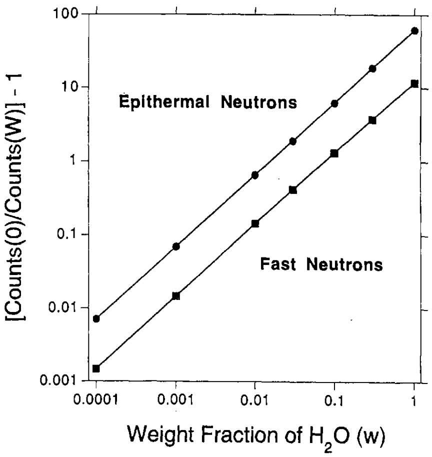

Fig. 2. Simulated epithermal and fast-neutron counting rates as a function of mass fraction of H_2O (*w*), added to a FAN regolith.

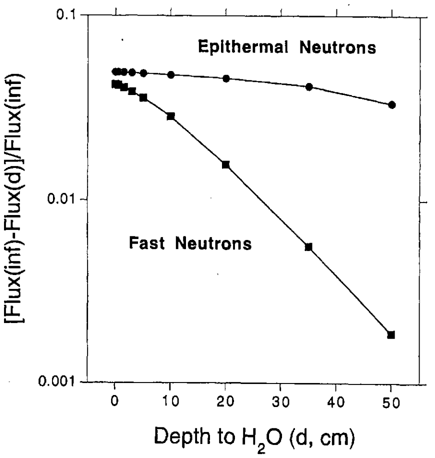

Fig. 3. Simulated epithermal and fast-neutron counting rates for a desiccated FAN layer of varying thickness *d* that overlays a thick, circular deposit of water ice having a radius of 24.3 km, which is surrounded by a desiccated FAN regolith. Here and throughout this study, a density of 2 g cm^{-3} is assumed. Also, inf is an effectively infinite depth.

correspond to low or thermal, intermediate or epithermal, and high or fast neutrons, which reflect the neutron production and energy moderation process. Fast neutrons are formed at high energies as the result of interactions between galactic cosmic rays and the nuclear constituents of the regolith. They transfer energy to nuclei in the regolith at a nearly constant fractional rate during subsequent, primarily elastic scattering collisions. This process results in an epithermal flux spectrum that is proportional to E^{-1} [or constant $L(E)$]. As their energy approaches that of the thermal motion of regolith nuclei, they begin to absorb energy as fast as they lose it and thereby develop a Maxwellian velocity distribution (the peaks at the lowest energies in Fig. 1). The thermal-neutron population builds in amplitude until the rate of injection from the fast-neutron population equals the rate of absorption due to thermal capture reactions plus the rate of loss to space.

The dominant effect of hydrogen (here assumed to be in the form of water molecules) is to monotonically decrease the intensity of epithermal and fast neutrons (Fig. 1). In contrast, the effect of hydrogen on the thermal population is not monotonic, producing a maximum between about 3 and 5 weight % of H_2O. Also, all the spectra slope downward toward lower energies in the epithermal range because of the absorption of neutrons by regolith nuclei at the rate

$$R_a = [\Sigma N_i \sigma_{ai}] V_n, \qquad (1)$$

where the sum is over all regolith elements *i*, N_i is the number density of element *i*, and σ_{ai} is the cross section for absorption of a neutron having velocity V_n by element *i*. This rate is independent of neutron energy because, for most elements, $V_n \sigma_{ai}$ is constant. The number of neutrons absorbed in the epithermal range then depends only on the time they spend losing energy between the fast- and thermal-neutron energy ranges. Because this time decreases with increasing hydrogen content, the spectra flatten out as the weight percent of water increases from 0 to 100% (Fig. 1).

Instrumentation and data reduction. Neutrons were measured with three different spectrometers aboard LP (*18*). Thermal and epithermal neutrons were detected with two 5.7-cm-diameter by 20-cm-long ^{3}He gas-filled proportional counters pressurized to 10 atm. One detector was covered by a 0.63-mm-thick sheet of Cd and was sensitive only to epithermal neutrons [labeled ^{3}He(Cd) in Fig. 1]. The second was covered by a 0.63-mm-thick sheet of Sn. Both sensors were matched so that the difference in their counting rates provided a measure of the flux of thermal neutrons (labeled "thermal" in Fig. 1). Fast neutrons were measured with the anticoincidence shield (ACS) of the gamma-ray spectrometer (GRS). Here, events consisting of a time-correlated pair of interactions were used to positively identify fast neutrons. The pulse height of the first of the pair provided a measure of their energy spectrum between about 0.5 and 8.0 MeV (*18*).

The trend of decreasing $L(E)$ with increasing water content at epithermal energies was simulated by integrating the product of the energy spectra (Fig. 1) and the efficiency of the ^{3}He(Cd) sensor (Fig. 2). A similar calculation was made for fast neutrons with the efficiency function estimated for the ACS of the GRS (*19*, *20*). Epithermal and fast-neutron counting rates (epi-counts and fast-counts, respectively) can be represented by functions of the form

$$\text{epi-counts}(w) = \text{epi-counts}(0)/[1 + (61 \times w)], \qquad (2)$$

$$\text{fast-counts}(w) = \text{fast-counts}(0)/[1 + (12 \times w)], \qquad (3)$$

where *w* is the weight fraction of H_2O. These relations illustrate the large measurement advantage provided by epithermal neutrons in detecting small amounts of hydrogen. A 1% measurement precision corresponds to a hydrogen weight fraction of $[0.01/(61 \times 9)] = 18 \times 10^{-6}$. We verified (but do not show here) that these spectra and counting rates are not affected by a change in the composition from FAN to norite (another major type of rock abundant in the regolith in the lunar highlands). The fractional reduction in the epithermal-neutron counting rate is a factor of 5 higher than that for the fast-neutron counting rate.

The trend shown in Figs. 1 and 2 for an assumed surface stratigraphy that has infinite horizontal spatial extent does not represent the case for spatially confined deposits of enhanced hydrogen. Spatially confined deposits are expected if water ice resides in permanently shaded craters near both lunar poles. The results of a series of simulations for circular deposits of pure water ice having a radius of 24.3 km, which is surrounded by a desiccated FAN regolith and covered over by a layer of the same regolith of varying thickness *d*, are shown in Fig. 3. For water deposits that are small compared with the spatial response function of the sensor (as chosen for these simulations), the depression in epithermal and fast-neutron counting rates for thin cover layers (*d* less than ~10 cm) saturates at a value that is governed by the solid angle of the deposit as seen by the sensor. The relative solid angle for an assumed circular water deposit having a radius of 24.3 km is seen to be about 5%, which is consistent with a foot point size for the epithermal-neutron sensor of 37,100 km^2.

The percentage of reduction in the epithermal counting rate drops off slowly with increasing burial depths, whereas that in the fast-neutron counting rate drops by a factor of 2 for a burial depth of 15 cm (assuming a density of 2 g cm^{-3}) and a factor of 20 for 50 cm. This difference reflects the decreasing cross section of hydrogen for elastic neutron scattering as a function of increasing neutron energy. Beyond about 1 MeV, the cross section for hydrogen becomes less than that for oxygen. Because of this effect, overlying desiccated layers of regolith (which contain about 45% by mass of oxygen) will effectively screen buried hydrogen-rich layers from detection by fast neutrons.

Observations. The LP neutron data analyzed and reported here cover the period between 16 January and 27 June 1998. Epithermal and thermal counting rates were constructed from sums of ^{3}He(Cd) and ^{3}He(Sn) pulse-height spectra measured every 32 s (*18*) over a range of channels that bracket the 763-keV peaks of the ^{3}He(n,p)t reaction. These peaks correspond to detection of low-energy neutrons. Fast-neutron counting rates were generated by summing all background-subtracted, correlated double-interaction events detected in the ACS of the GRS [see (*18*) for details]. Counts were mapped with nearly equal area pixels, each having a bin size equal to that contained within a 2° latitude by 2° longitude box at the equator. All pixel counts were normalized to a constant neutron production rate by galactic cosmic rays with the intensity of the 6.13-MeV oxygen gamma-ray line measured by the LP GRS. Corrections were also made for the latitudinal dependence of instrument-response functions.

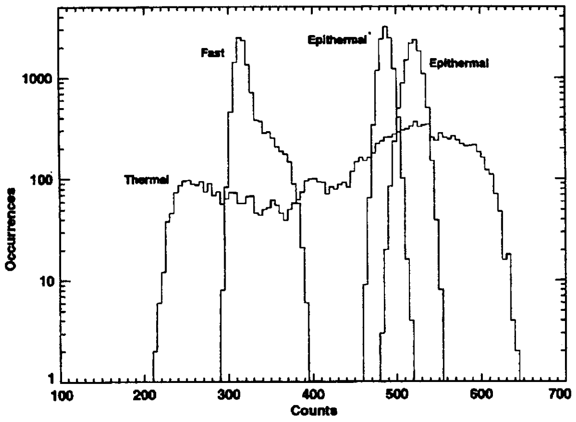

Fig. 4. Histograms of counts per areal pixel of thermal, epithermal, and fast-neutron counting rates. The histogram labeled "epithermal*" is constructed by subtracting 6.8% of the thermal histogram from the epithermal histogram.

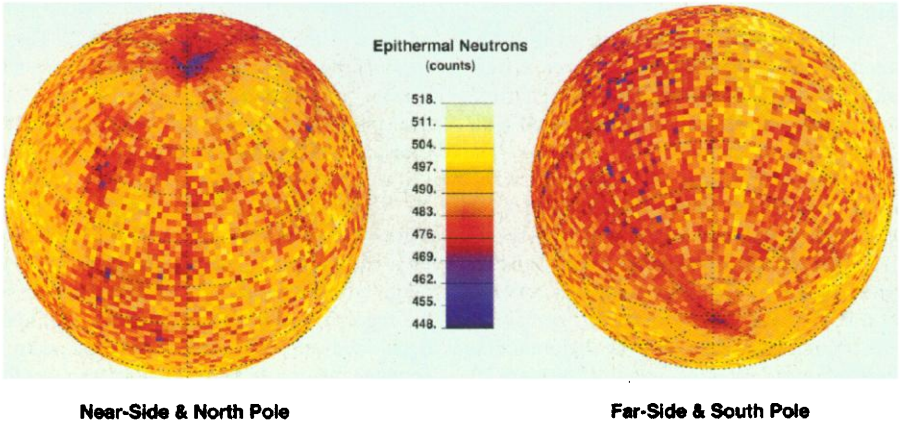

Fig. 5. A full-moon map of the epithermal* counting rates. Both globes are tilted by 45° in latitude with the nearside and North Pole at the left and the farside and South Pole at the right. The scale given in the middle corresponds to the counts registered by the Cd-covered ^{3}He gas proportional counter in 32 s.

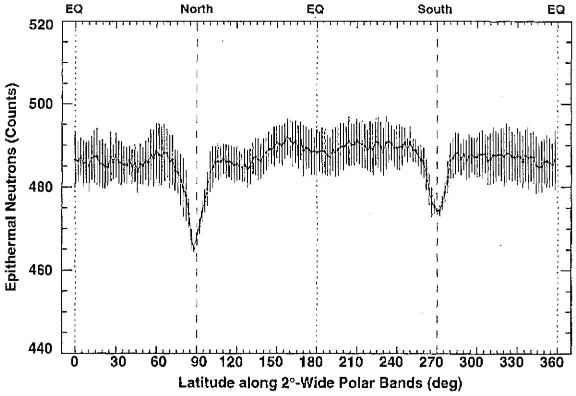

Fig. 6. Averages and standard deviations of all epithermal* counts for all equal area pixels in Fig. 5 within successive 2° wide latitude bins that are bounded in azimuthal angle by planes that are parallel to the lunar polar axis and separated by 2° in longitude at the equator (EQ).

Histograms of thermal, epithermal, and fast-neutron counts (Fig. 4) show that the epithermal counting rate distribution is narrower than those for the thermal and fast neutrons. This narrow distribution reflects the relatively low sensitivity of epithermal neutrons to composition (*21*). Their residual sensitivity can be reduced further with Eq. 1, which for all elements except Gd and Sm applies equally to thermal and epithermal neutrons. Effects of composition on epithermal counting rates can therefore be minimized by subtracting a fraction of the measured thermal counting rate. We found that histograms of epithermal-neutron counts have a minimum width if this fraction is 6.8%, which we use to define the population of epithermal* neutrons [epithermal* = epithermal − (0.068 × thermal)]. Comparison of both epithermal histograms reveals that the width of the epithermal* histogram is narrower, as evidenced by the increase in peak amplitude (for the same number of epithermal pixel counts). The effect is more noticeable in the full map of epithermal counting rates. Whereas the epithermal map (not shown here) contains shadows that enclose the maria, which are outlined in a map of the thermal neutrons [figure 2 of (*22*)], these shadows are much reduced in the map of epithermal* neutrons (Fig. 5). In addition, two concentrations of dark pixels are visible at the lunar poles, which are neither circular nor centered on the poles.

Longitudinal averages of epithermal* counting rates as a function of latitude (Fig. 6) show only two prominent minima, one at the North Pole and one at the South Pole. The fractional decreases in polar counting rates have slightly different shapes and are both offset from the poles. Although not demonstrated here, both depressions are broader than the spatial response function of the epithermal-neutron sensor. Whereas the peak of the depression at the north is 4.6% relative to neighboring latitudes within about ±30° of each minimum, that at the south is 3.0%. An integration of epithermal counting rates poleward of ±85°

yields fractional depressions in epithermal* counting rates of 3.0 and 2.6% relative to the full moon value, at the North and South Poles, respectively. A similar calculation poleward of ±80° yields fractional depressions of 2.0 and 1.6%, respectively.

A map of fast-neutron counting rates [figure 3 of (*22*)] shows no evident decrease in the fast-neutron flux at either pole that is consistent with the decreases in flux observed in the epithermal* map of the moon (Fig. 5). This perception is quantified by constructing longitudinal averages and their standard deviations of the fast-neutron counts as a function of latitude (Fig. 7). Although no substantial effect is seen, we can use these data to establish an upper limit for fast neutrons by comparing the lowest counting rate within ±5° of each pole with a smoothed interpolation of counts within a ±30° range of each pole. This procedure gives upper-limit relative fast-neutron flux decreases of 0.35% in the north and 0.5% in the south. The statistical precision of averaged counts at both poles is 0.25%. The effect in fast neutrons is therefore more than about a factor of 10 smaller than that seen in epithermal* neutrons.

Support for interpretation of the enhanced deposits of hydrogen evident in epithermal-neutron data in terms of water ice is given by comparing the locations of observed decreases in epithermal* counting rates with locations of permanently shaded polar areas (Fig. 8). The largest decreases of counting rates in the north (shown by the colors between purple and magenta) are seen to cover the north-facing rim of Peary crater and a linear trend parallel to the +130° meridian that extends to +77° latitude. They also cover parts of the rims of the Hermite, Rozhdestvenskiy, and Plaskett craters. The largest decreases in the south (shown in purple) are close to the pole but on the nearside of the rim of the South Pole–Aitken basin. Reduced counting rates (shown in blue) follow a linear trend along the −50° to +130° meridian and also cover patches of the rim of the Schrodinger crater. Comparison with Clementine 750-nm images (*23*) shows that all of these locations contain many (unresolved by the NS) small areas that appear to be in permanent shadow.

Discussion. Comparison of the upper-limit ratio of fast to epithermal depressions in counting rates at both poles (about a factor of 10) with the simulations (Fig. 3) shows that LP epithermal and fast-neutron data are consistent with models of buried water-ice deposits. If accumulation of more fast-neutron data in succeeding LP map cycles confirms our present upper-limit estimate as real depressions, then the measured epithermal- and fast-neutron fluxes are consistent with theoretical expectations for pure water-ice deposits buried beneath a dry regolith having a thickness of about 40 cm. These deposits would then have total effective surface areas of about 1850 km^2 at both poles.

This model is not unique because similar results could be obtained with different combinations of (i) lower water-ice abundances in the buried deposit, (ii) different surface area and surface distribution of the deposit, (iii) different burial depth below dry regolith, and (iv) a multilayered geometry containing alternate layers of water ice and dry regolith. This last configuration could result from a series of comet impacts that occurred at different times in the past.

If our interpretation of the LP neutron data is correct, a partially buried water-ice deposit is consistent with interpretations of existing radar backscatter data (*24*). These data provide only questionable evidence for polar water ice on the moon, including areas that are within the few permanently shaded lunar craters that are visible to Earth-based radar [see, for example, (*24*) and references therein]. These null observations are consistent with the presence of buried water ice because the Fe and Ti abundance of lunar regolith at its poles is sufficiently high (*25*) to absorb backscatter radar signals from water-ice deposits that are buried at depths by more than about 20 cm (*26*).

We can estimate the amount of water ice that may be found in permanently shadowed polar areas if we assume that (i) the ice deposits are below a 40-cm-thick layer of dry regolith, (ii) they are pure water ice, (iii) they reach a depth of 2 m, that is, the depth estimated to be gardened in 2 billion years (*3*), and (iv) the surface area of permanently shadowed crater deposits is 1850 km^2 at each pole as simulated above. Then each polar region could contain as much as roughly 3×10^9 metric tons of water ice. This amount is about an order of magnitude less than that predicted as possibly delivered to and retained on the moon by comets over the past 2 billion years (*3*).

This estimate may be wrong by a large factor if the actual area in permanent shadow at both poles differs from our assumed value of 1850 km^2. Estimates based on Clementine data (*12*, *23*) yield 530 km^2 north of +87.5° and 6361 km^2 south of −87.5° latitude. There is a potential inconsistency here because the measured epithermal-neutron effect is larger in the north, yet the permanently shaded area appears to be larger in the south. This discrepancy implies either that all of the excess hydrogen is not in the form of water ice or that the permanently shaded areas estimated from Clementine data do not represent con-

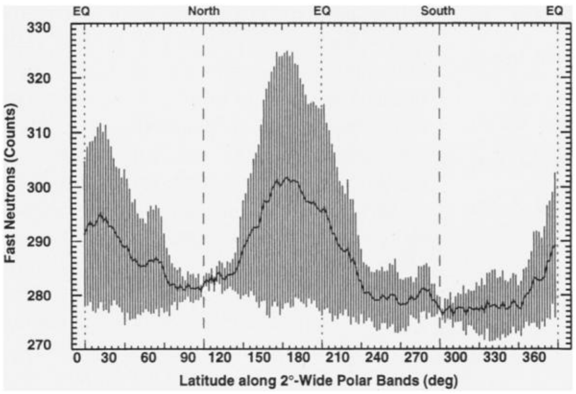

Fig. 7. Averages and standard deviations of all fast-neutron counts for all equal area pixels in figure 3 of (*22*) within successive 2° wide latitude bins that are bounded in azimuthal angle by planes that are parallel to the lunar polar axis and separated by 2° in longitude at the equator.

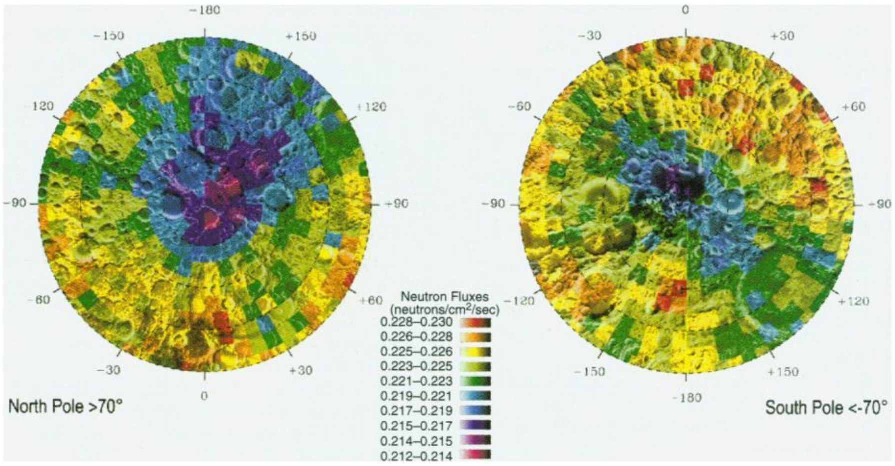

Fig. 8. Overlay of epithermal* counting rates in each 2° by 2° equal area pixel poleward of ±70° with surface relief maps of the lunar poles (*28*).

ditions near the poles at latitudes equatorward of ±87.5°. This last possibility is supported by the fact that the South Pole of the moon was viewed by Clementine during winter. Areas that appear to be shaded during the winter months may receive sunlight during other times of the year.

However, it is also possible that some of the excess hydrogen inferred from epithermal*-neutron data near the lunar poles is dispersed throughout relatively large areas of the polar regolith, having been delivered to the moon at more equatorial latitudes by the solar wind but transported to the poles through multiple collisionless hops through the lunar exosphere (*2*–*6*). By the method of construction, our polar estimates made from Fig. 6 are additions to the average mass fraction of hydrogen implanted in the regolith by the solar wind at lower latitudes. We believe a solar wind for most of the observed excess hydrogen is unlikely because the lack of a fast-neutron signature rules against a surface deposit.

References and Notes

1. D. Vaniman *et al.*, in *Lunar Sourcebook, a User's Guide to the Moon*, G. H. Heiken, D. T. Vaniman, B. M. French, Eds. (Cambridge Univ. Press, Cambridge, 1991), pp. 5–26.
2. K. Watson, B. C. Murray, H. Brown, *J. Geophys. Res.* **66**, 3033 (1961).
3. J. R. Arnold, *ibid.* **84**, 5659 (1979).
4. R. R. Hodges Jr., *Proc. Lunar Planet. Sci. Conf.* **11**, 2463 (1980).
5. A. P. Ingersoll, T. Svitek, B. C. Murray, *Icarus* **100**, 40 (1992).
6. B. J. Butler, *J. Geophys. Res.* **102**, 19283 (1997).
7. L. J. Lanzerotti, W. L. Brown, R. E. Johnson, *ibid.* **86**, 3949 (1981).
8. T. H. Morgan and D. E. Shemansky, *ibid.* **96**, 1351 (1991).
9. M. A. Slade, B. J. Butler, D. O. Muhleman, *Science* **258**, 635 (1992).
10. J. K. Harmon and M. A. Slade, *ibid.*, p. 640.
11. B. J. Butler, D. O. Muhleman, M. A. Slade, *J. Geophys. Res.* **98**, 15003 (1993).
12. S. Nozette *et al.*, *Science* **274**, 1495 (1996).
13. R. A. Simpson and G. L. Tyler, in preparation.
14. N. J. S. Stacy, D. B. Campbell, P. G. Ford, *Science* **276**, 1527 (1997).
15. W. C. Feldman *et al.*, *J. Geophys. Res.* **98**, 20855 (1993).
16. W. C. Feldman *et al.*, *ibid.* **102**, 25565 (1997).
17. Lethargy is the neutron flux as a function of logarithmic energy interval, $L(E) = E \times F(E)$, where E is the neutron energy and $F(E)$ is the neutron flux.
18. W. C. Feldman *et al.*, *Nucl. Instrum. Methods Phys. Res. A*, in press.
19. R. C. Byrd and W. T. Urban, *LANL Doc. LA-12833-MS* (Los Alamos National Laboratory, Los Alamos, NM, 1994).
20. W. C. Feldman, G. F. Auchampaugh, R. C. Byrd, *Nucl. Instrum. Methods Phys. Res. A* **306**, 350 (1991).
21. W. C. Feldman, R. C. Reedy, D. S. McKay, *Geophys. Res. Lett.* **18**, 2157 (1991).
22. W. C. Feldman *et al.*, *Science* **281**, 1489 (1998).
23. E. M. Shoemaker, M. S. Robinson, E. M. Eliason, *ibid.* **266**, 1851 (1994).
24. J. K. Harmon, *Adv. Space Res.* **19** (no. 10), 1487 (1997).
25. R. Jeanloz, D. L. Mitchell, A. L. Sprague, I. de Pater, *Science* **268**, 1455 (1995).
26. B. J. Butler, thesis, California Institute of Technology, Pasadena (1994).
27. R. E. Alcouffe *et al.*, *LANL Manual LA-7369-M*, rev. 2 (Los Alamos National Laboratory, Los Alamos, NM, 1995).
28. U.S. Geological Survey (USGS), Surface-relief maps of the lunar poles (USGS, Flagstaff, AZ, 1981).
29. We thank B. C. Murray, M. A. Slade, H. Wänke, J. K. Harmon, and R. R. Vondrak for many stimulating conversations regarding the interpretation of our results.

Supported in part by Lockheed-Martin under contract to NASA and conducted under the auspices of the U.S. Department of Energy.

13 July 1998; accepted 10 August 1998

Low-Temperature Synthesis of Zintl Compounds with a Single-Source Molecular Precursor

Michael A. Beswick,* Nick Choi, Christopher N. Harmer, Alexander D. Hopkins, Mary McPartlin, Dominic S. Wright*

Thermolysis of the heterobimetallic phosphinidene complex $\{[Sb(PCy)_3]_2Li_6 \cdot 6HNMe_2\}$ ($Cy = C_6H_{11}$) at 303 to 313 kelvin gives Zintl compounds containing $(Sb_7)^{3-}$ anions. The complex thus constitutes a stable molecular single-source precursor to Zintl compounds and provides a potential low-temperature route to photoactive alkali metal antimonates. The new chemical reaction involved, which is driven thermodynamically by the formation of P–P bonds, has implications in the low-temperature synthesis of other technologically important materials (such as gallium arsenide).

Zintl compounds, which contain polyatomic posttransition metal anions and alkali or alkaline earth metal cations, were discovered over a hundred years ago (*1*). In the 1930s, Zintl and co-workers investigated the composition of solutions of group 14 or 15 elements with alkali metals in liquid NH_3 and showed that, depending on the concentration, a wealth of polyatomic main-group anions are present in equilibrium (*2*). To control their stoichiometry and to obtain single components, direct dissolution of binary alloys of the alkali and posttransition elements (prepared typically at 873 to 1473 K) is required (*3*). Corbett and others have used 2,2,2-crypt-[4,7,13,16,21,24-hexaoxa-1,10-diazabicyclo-(8,8,8)hexacosane], which strongly complexes Na^+ and K^+ cations and separates them from the polyatomic anions, to provide stable crystalline materials that are amenable to x-ray structural determination (*4*). Such structural investigations revealed that a wealth of bonding patterns are adopted by the polyatomic posttransition metal anions and these studies have had a fundamental impact on modern bonding theory (*4*).

Recently, by using stepwise metallation of primary amines and phosphines, we showed that a variety of heterometallic alkali metal/Sb(III) imido and phosphinidene complexes are accessible (*5*, *6*). We report here that thermolysis of the heterobimetallic phosphinidine complex $\{[Sb(PCy)_3]_2Li_6 \cdot 6HNMe_2\}$ **1** ($Cy = C_6H_{11}$) (*6*) in toluene at 303 to 313 K gives the Zintl compound $[Sb_7Li_3 \cdot 6HNMe_2]$ **2** and, with excess TMEDA, it gives $[\{(TMEDA)Li\}_3 Sb_7] \cdot$toluene **3** [TMEDA= $(Me_2NCH_2)_2$] (*7*). The isolation of $(CyP)_4$ from these reactions indicates that this process involves reductive elimination (*7*), with the formation of P–P bonds (having the highest bond energy between any group 15 elements) providing the thermodynamic driving force. Complex **1** thus constitutes a stable molecular single-source precursor to Zintl compounds.

Low-temperature x-ray studies of **2** (Fig. 1) and **3** (Fig. 2) (*8*) show that they consist of discrete heterobimetallic cage molecules in which $(Sb_7)^{3-}$ ions are complexed at the equatorial Sb atoms by three Lewis base solvated Li^+ cations. The Sb–Li bond lengths in both complexes (average 2.92 Å in **2** and 2.89 Å in **3**) are comparable with those found in the other known Sb–Li bonded complexes (*9*–*11*). The minor differences in the bond lengths and angles observed in the $(Sb_7)^{3-}$ anion of **2** and **3** compared with the previously reported ion-separated complexes (*12*, *13*) imply that only weak Sb–Li bonding is occurring here. The recent synthesis of the only other Li/Sb Zintl compound, $[Li(NH_3)_4]_3[(NH_3)_2Li_2Sb_5]$, containing the cyclic $(Sb_5)^{5-}$ anion from the direct reaction of metallic Li and Sb in liquid ammonia is of particular relevance here (*11*). The same $[Sb_7]^{3-}$ ion is formed by thermolysis of **1** as is produced by addition of 2,2,2-crypt or ethyl-

---

M. A. Beswick, C. N. Harmer, A. D. Hopkins, D. S. Wright, Department of Chemistry, Lensfield Road, Cambridge CB2 1EW, UK. N. Choi and M. McPartlin, School of Chemistry, University of North London, London N7 8DB, UK.

*To whom correspondence should be addressed. E-mail: dsw1000@cus.cam.ac.uk